TRENDS IN SCIENCES 2026; 23(8): 12650
https://doi.org/10.48048/tis.2026.12650
RESEARCH ARTICLE

Preparation of Fe-doped Silicalite-1 Using Geothermal Sludge as a Potential Adsorbent for Methylene Blue Removal

Ade Irma Rozafia[1], Bintang Prameswara[1], Nur Karimah[1], Nor Farida[1], Wahyu Prasetyo Utomo[1], Ratna Ediati[1], Aishah Abdul Jalil[2,3] and Djoko Hartanto[1,*]

[1]Department of Chemistry, Faculty of Science and Data Analytics, Institut Teknologi Sepuluh Nopember (ITS), Surabaya 60111, Indonesia
[2] Centre of Hydrogen Energy, Institute of Future Energy, 81310, UTM Johor Bahru, Johor, Malaysia
[3]Faculty of Chemical and Energy Engineering, Universiti Teknologi Malaysia, 81310, UTM Johor Bahru, Johor, Malaysia

([*]Corresponding author's e-mail: djokohar@its.ac.id)

Received: 14 November 2025, Revised: 22 December 2025, Accepted: 10 January 2026, Published: 20 March 2026

Abstract

Geothermal sludge contains a high concentration of silica (85% - 93%) that is typically waste in geothermal plant, offering a promising alternative silica precursor for synthesizing of silicalite-1. In this study, geothermal sludge was acid-leached to remove impurities and enrich reactive silica, then used for hydrothermal preparation of Fe-doped silicalite-1 with Fe addition of 0.002 - 0.014 mol. Low Fe loading preserved the MFI framework with only a slight reduction in relative crystallinity (Fe@S-2 = 95.81%), whereas excessive Fe loading largely suppressed MFI formation (Fe@S-14 = 1.77%) and produced a partially amorphous material. The as-prepared Fe@S-5 exhibited a spherical morphology with an average particle size of 2.89 µm and the external surface area increased with Fe loading, reaching 174.2 $m^2 g^{-1}$ for Fe@S-14. In methylene blue adsorption, Fe@S-14 showed the highest uptake of 46 mg g^{-1} compared with S-1 of 7.9 mg g^{-1}. The adsorption kinetics followed the pseudo-second order model and equilibrium data were reasonably described by the Langmuir isotherm within the investigated concentration range. Overall, this work demonstrates a sustainable route to utilize geothermal sludge into functional adsorbents for dye-containing wastewater treatment with clear potential for industrial implementation.

Keywords: Geothermal sludge, Hydrothermal synthesis, Fe-doped silicalite-1, Adsorption, Methylene blue, Sustainable silica source

Introduction

Zeolites are crystalline microporous framework materials widely used in catalysis, adsorption, and separation due to their uniform pore size distribution, ion exchange capacity, structural tunability can be tailored for specific applications [1-4]. Furthermore, performance is often enhanced by introducing heteroatom or metal species to introduce additional active sites and modify surface heterogeneity [5]. Among all-silica zeolite, silicalite-1 is particularly attractive for treating organic pollutants due to its high thermal stability and hydrophobicity, and tunable surface properties, which favor the uptake of organic molecules from aqueous media [6].

Silicalite-1 is commonly synthesized hydrothermally using tetraethyl orthosilicate (TEOS) and tetra propylammonium (TPA) as the structure-directing agent [7]. However, the cost and non-renewable environment of TEOS restrict the sustainability and large-scale feasibility of silicalite-1 production. Consequently, waste product has emerged as an alternative feedstock for synthesizing porous materials, offering potential cost reduction and environmental benefits through waste utilization [8]. In

this context, geothermal sludge formed from silica scaling and accumulated in geothermal power plants that consists of 165 ton per month especially at the Dieng power plant in Indonesia while its utilization is minimal. The solid residue from geothermal sludge contains 90-98% amorphous silica, which serves as a suitable source material for the synthesis of zeolite [9]. Ilman *et al.* [10] reported that geothermal sludge contains up to 95.70 wt% SiO_2, accompanied by impurities such as Fe_2O_3, CaO, K_2O, TiO_2, Na, Cl, and others. These impurities can interfere with zeolite crystallization and must be controlled to enable reliable synthesis and reproducible properties. Acid leaching is a practical pre-treatment to reduce these impurities and enrich reactive silica, among different acids, HCl is frequently reported as effective for dissolving metal contaminants while preserving the silica structure [11]. Importantly, converting geothermal sludge into a reactive silica precursor therefore represents a promising route to produce value added zeolitic materials while reducing disposal burdens and dependence on commercial silica sources [12].

In parallel, Fe doped into zeolite framework has attracted attention due to iron is abundant, relatively low in toxicity, and can introduce additional adsorption sites and surface heterogeneity relevant to environmental remediation [13]. Zhai et al. used TEOS as silica precursor, successfully synthesized iron containing hollow MFI zeolites by hydrothermal method [14]. Guo *et al.* [15] reported a hydrothermal method to successfully synthesize encapsulated Fe nano catalyst inside silicalite-1 and exhibited significantly improved catalytic activity and reusability in the catalytic degradation process of methylene blue. Radoor *et al.* [16] reported synthesis of silicalite-1 for adsorption MB using TEOS as silica precursor can exhibit 86% removal efficiency even after 6 adsorption-desorption cycle. Nevertheless, most Fe-doped silicalite-1 reported to date still relies on commercial silica precursors, limiting the sustainability and economic attractiveness of scale-up. Moreover, although waste by product (e.g., fly ash) has been used to produce silicalite-1 [17], the direct use of geothermal sludge for synthesizing Fe-doped silicalite-1 remains insufficiently explored, and the influence of Fe loading on crystallization behavior, textural development, and adsorption performance has not been systematically established. We hypothesize that acid leaching of geothermal sludge produces a sufficiently reactive and low impurity silica source to enable reproducible MFI-type silicalite-1 crystallization. We further propose that Fe addition during synthesis modifies the silica network by increasing surface heterogeneity, creating Fe-associated sites that improve the accessibility of adsorption sites, thereby enhancing methylene blue uptake.

Accordingly, this study aims to synthesize silicalite-1 and Fe-doped silicalite-1 using acid-leached geothermal sludge as the primary silica precursor via hydrothermal crystallization, quantify the effects of Fe loading on phase composition/ crystallinity, evaluate methylene blue adsorption performance using experimental uptake, isotherm and kinetic parameters. This work is expected to reduce dependence on TEOS, lowers precursor cost, and mitigates geothermal waste disposal, offering a more sustainable and scalable route to adsorbents for dye contaminated wastewater treatment.

Materials and methods

Materials

The materials used in this study included geothermal sludge obtained from the Indonesian Geothermal Plant, hydrochloric acid (HCl, Smartlab, 37%), tetrapropylammonium bromide (TPABr, Merck, 98%), iron(III) nitrate nonahydrate ($Fe(NO_3)_3 \cdot 9H_2O$, Merck, 98%), methylene blue ($C_{16}H_{18}ClN_3S$, Merck), sodium hydroxide (NaOH, Sigma-Aldrich, 97%), and deionized water.

Silica extraction from geothermal sludge

The 4 g of geothermal sludge obtained from Indonesia geothermal plant was first oven-dried at 105 °C overnight and then ground using a mortar to obtain a fine powder. The dried sludge was carried out to acid leaching using 40 mL of 2 M HCl at 90 °C for 5 h under continuous stirring at 350 rpm in a fume hood to remove metal impurities such as Fe_2O_3, K_2O, and CaO. The solid residue was separated by filtration, thoroughly washed with deionized water until neutral pH was reached, and then dried at 105 °C overnight. The purified material was subsequently dissolved in 20 mL of 6 M NaOH solution and stirred at 350 rpm for 6 h at 90 °C to extract silicate species. The resulting sodium

silicate solution was subsequently used as the silica precursor for zeolite synthesis.

Preparation for silica sol

Silica sol was prepared from the SiO_2 extracted solution obtained via alkaline extraction of geothermal sludge. First, 4.32 mL of sodium silicate solution was filtered to remove any residual solid impurities. The pH of the filtration was then adjusted to 1 by adding 8 mL of 2 M HCl under continuous stirring at 350 rpm to induce silica gel formation. The resulting gel was aged for 36 h at 75 °C to promote polymerization and particle growth. To prepare the silica sol, 2.16 mL of SiO_2 extract was diluted in 25 mL of deionized water, followed by the addition of 1.17 g of the as-prepared silica gel. The mixture was stirred at 350 rpm at ambient temperature for 3 h to ensure homogeneity. The suspension was subsequently transferred to a Teflon-lined autoclave and hydrothermally treated at 65 °C for 24 h to obtain a stable silica sol. The resulting sol was used as the silica precursor for the hydrothermal synthesis of Fe-doped silicalite-1.

Hydrothermal synthesis of Fe-doped silicalite-1

Fe-doped silicalite-1 was synthesized via a hydrothermal method reported by Yang *et al.* [7], with modifications. The synthesis gel composition was $1.0SiO_2$: 0.04TPABr: $0.2Na_2O$: $50H_2O$: xFe (x = 0.002, 0.005 and 0.014 mol). First, 0.326 g of tetra propylammonium bromide (TPABr) was dissolved in 16 mL of deionized water. Separately, the required amount of $Fe(NO_3)_3 \cdot 9H_2O$ was dissolved in 10 mL of deionized water until a clear and homogeneous solution was obtained. The silica sol was added to the TPABr solution, followed by the dropwise addition of the $Fe(NO_3)_3 \cdot 9H_2O$ solution under continuous stirring at 350 rpm. The pH of the resulting mixture was monitored and adjusted to 10 by adding 1 M HCl. The gel was stirred for 3 h at ambient temperature to ensure homogeneity, then transferred to a Teflon-lined stainless-steel autoclave and aged for 13 h. The hydrothermal crystallization was carried out at 150 °C for 24 h. After crystallization, the solid product was collected by filtration, thoroughly washed with deionized water until pH neutral, and dried at 75 °C for 24 h. The dried samples were calcined at 550 °C for 6 h under N_2 atmosphere to remove the organic template and obtain the final Fe@Sx materials. The Fe content was varied at molar ratios of 0.002, 0.005, 0.014 and the resulting samples were labelled as Fe@S-2 (0.002), Fe@S-5 (0.005), and Fe@S-14 (0.014), respectively. Silicalite-1 synthesized under the same conditions without Fe addition was denoted as S-1. A schematic illustration of the Fe-doped silicalite-1 synthesis was shown in **Figure 1**.

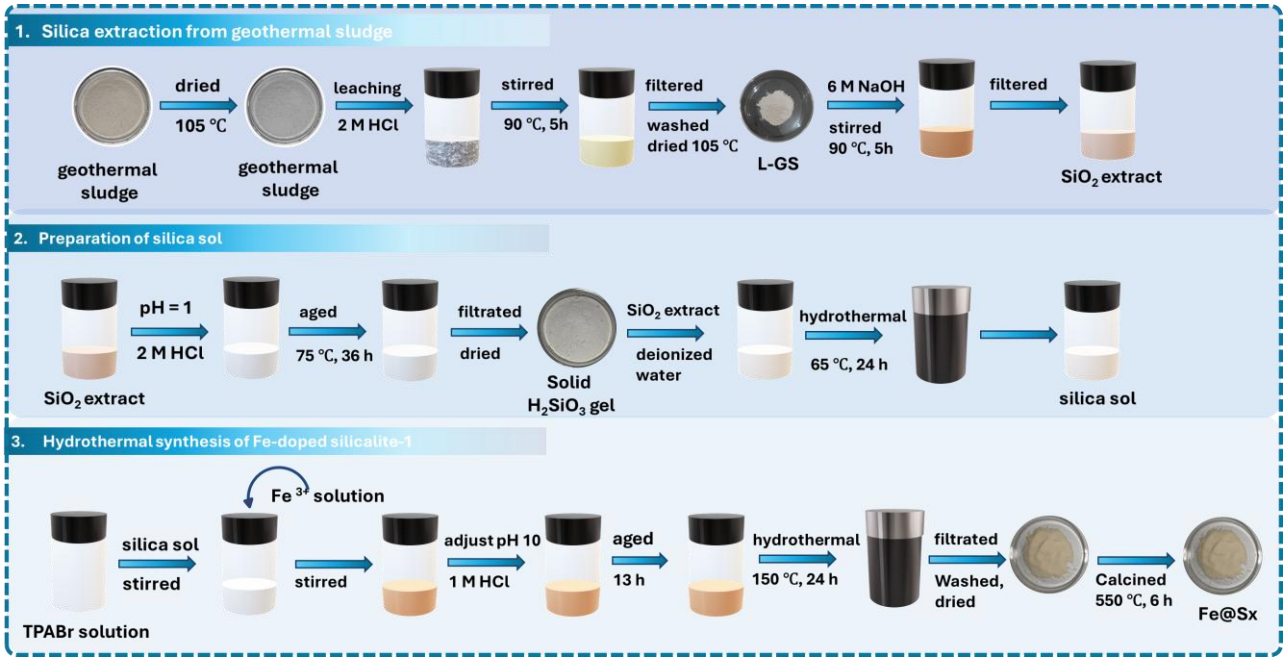

Figure 1 Schematic illustrations of synthesis of Fe-doped silicalite-1 from geothermal sludge.

Characterization

The structural, chemical, and morphological properties of the synthesized materials were analyzed using several characterization techniques. The elemental composition of the raw geothermal sludge was determined using X-ray fluorescence (XRF, PANalytical type Prodigi), with accelerating voltage 30 kV. Crystal phase and crystallinity structure of the synthesized samples was characterized by X-ray diffraction (XRD) [18]. The XRD analysis was performed using XRD PANalytical under Cu Kα irradiation (λ = 1.5406 Å) with the diffraction angle of 2θ = 10° - 65° and accelerating voltage and current of 40 kV and 15 mA, respectively. Fourier-transform infrared spectroscopy using Shimadzu IRAFFINITY-s at 400 - 4,000 cm^{-1} using conventional KBr pellets to identify functional groups [19,20]. The surface morphology and elemental distribution were examined by field-emission scanning electron microscopy coupled with energy-dispersive X-ray spectroscopy (FESEM-EDX) Hitachi Regulus 8220 at 1.5 kV [21]. The surface area of the materials was measured using MB adsorption method as follows Eqs. (1) [22,23].

Equation of surface area by MB adsorption:

$$S = \frac{\left(\frac{x}{m}\right).\ N.\ \alpha}{Mw}) \quad (1)$$

where S is the surface area $m^2\ g^{-1}$, x/m is the amount of MB adsorbed per gram of adsorbent g g^{-1}, N is Avogadro's number (6.02×10^{23} particle/mol), α is the size of a single MB molecule (1.97×10^{-18}), and Mw is molecular weight MB (320.5 g mol^{-1}).

Adsorption experiment

The adsorption performance of the samples was evaluated using methylene blue (MB) as an organic dye. Typically, 0.03 g of adsorbent was added to 50 mL of an MB solution with varying concentration of MB 10, 20, 30 and 40 mg L^{-1} then stirred for 60 min at 350 rpm. During the adsorption process, 4 mL of the solution was taken every 15 min up to 60 min. The MB concentration was determined using a UV-Vis spectrophotometer at a wavelength of 655 nm. The adsorption capacity (q_t) and removal efficiency (R%) were calculated using standard mass-balance equations. The kinetic data were fitted using pseudo-first order and pseudo-second-order models, while adsorption isotherms were analyzed using Langmuir and Freundlich models to explain the adsorption mechanism and surface behaviour. The pseudo-first order and pseudo-second order models as follows: Eqs. (2) and (3), respectively.

Equation of pseudo-first order

$$q_t = q_e(1 - e^{-K_1 t}) \quad (2)$$

Equation of pseudo-second order

$$q_t = \frac{K_2 {q_e}^2 t}{1+K_2 q_e t} \quad (3)$$

where $q_t$is the adsorption capacity at time t(min) in mg g^{-1}, and $q_e$is the adsorption capacity at equilibrium (mg g^{-1}). The rate constants $K_1$and K_2represent the reaction rate constants for the pseudo-first order (PFO) and pseudo-second order (PSO) kinetic models, respectively. The non-linear forms of the Langmuir and Freundlich isotherm models can be expressed in Eqs. (4) and (5), respectively.

Equation of Langmuir isotherm model

$$q_e = \frac{q_m K_L C_e}{1+K_L C_e} \quad (4)$$

Equation of Freundlich isotherm model

$$q_e = K_f C_e^{1/n} \quad (5)$$

where $q_e$is the adsorption capacity at equilibrium (mg g^{-1}), and $q_m$represents the maximum adsorption capacity. $K_L$is the Langmuir isotherm constant related to adsorption affinity, while $K_F$is the Freundlich isotherm constant indicating adsorption capacity. The non-linear Langmuir and Freundlich isotherm plots are obtained by plotting the equilibrium concentration (C_e) on the x-axis and the adsorption capacity (q_e) on the y-axis.

Results and discussion

Identification of chemical composition of the geothermal sludge

The X-ray fluorescence analysis confirmed that SiO_2 was considered the primary component at around 85 wt%, while other metal oxides such as Al_2O_3, P_2O_5, CaO, Fe_2O_3, and K_2O were present in smaller quantities at 1 - 5 wt%. To improve silica purity and remove metal impurities, the geothermal sludge was subjected to acid leaching using 2 M HCl. Hydrochloric acid was selected due to it more efficiently dissolves metal contaminants than acids such as HNO_3, H_2SO_4, and H_3PO_4 [24]. The resulting filtrate had a yellowish-brown color, indicating effective leaching of metal impurities. The leached powder contained 93.9 wt% SiO_2 and was subsequently used as a high-purity silica precursor for zeolite synthesis as detailed in **Table 1**.

Table 1 Chemical composition of the geothermal sludge and acid treated sample.

Sample (%)	SiO_2	Al_2O_3	CaO	Fe_2O_3	P_2O_5	K_2O	Others
Geothermal sludge	85.0	4.6	3.5	3.3	1.3	0.8	0.4
Acid treated sample	93.9	1.3	1.3	1.6	0.8	0.3	0.1

Structural, morphological, and chemical properties

The XRD pattern of S-1 exhibits the characteristic peaks of the silicalite-1 at 2θ = 7.54°, 8.58°, 22.94°, 23.54°, and 24.04°, corresponding to the (101), (202), (501), (303), and (133) facets, proving the well-crystallized MFI framework [25,26]. The peaks observed at (101) and (202) facets indicate representative of pentasil units oriented parallel to the *ac*-plane, which underpin the linear and zig-zag channels system of the MFI structure. The diffraction pattern indicates a long-range ordering of the interconnected SiO_4 tetrahedral. Meanwhile, the diffraction peaks at 22.94°, 23.65°, and 24.04° indexed to the (501), (303), and (133) facets are commonly attributed to the local arrangement of SiO_4 tetrahedra forming 10-membered ring and channel intersections within the 3-dimensional zeolitic structure [27]. The XRD pattern of the Fe@S-2 and Fe@S-5 showed a similar diffraction to S-1, indicating that the MFI framework is largely preserved after Fe loading. The addition of Fe^{3+} into the silica framework is attributed to isomorphous substitution of Si^{4+}, which can occur without disrupting the MFI framework. The diffraction peaks in Fe@S-2 and Fe@S-5 shifted, indicating a uniform distribution of the Fe species within the MFI structure. In the Fe@S-14, significant structural and phase changes were observed through a broadening of the diffraction peak at 2θ = 23°. This result indicates the formation of an amorphous phase along with the destruction of the MFI structure in the material. The excessive Fe species can inhibit the nucleation and crystal growth of the MFI structure during the hydrothermal process. The XRD pattern indicates that the crystallinity and stability of the Fe@Sx are considerably affected by the Fe loading and its distribution within the MFI structure.

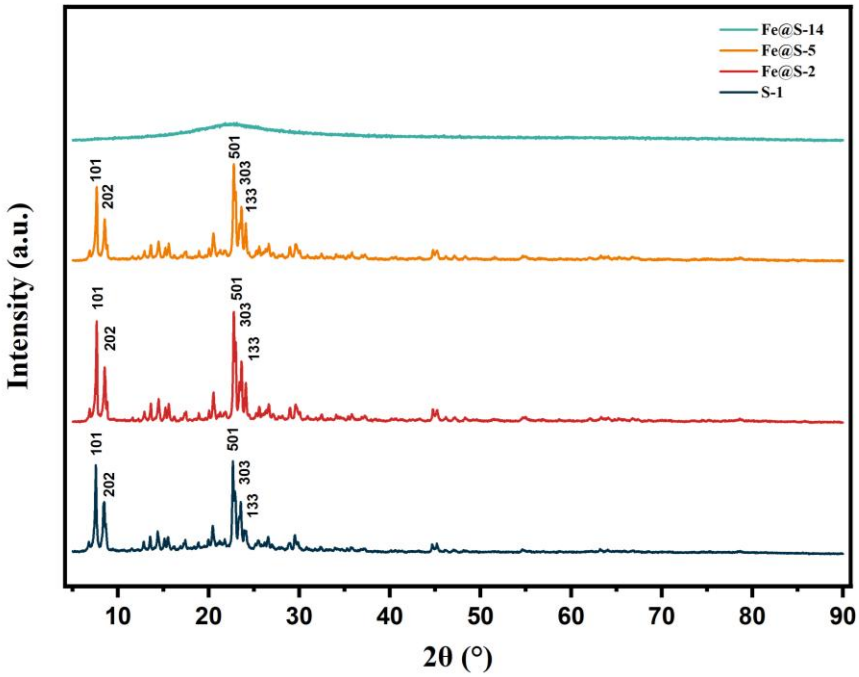

Figure 2 XRD patterns of silicalite-1 synthesized from geothermal sludge with different Fe molar ratio.

Table 2 summarizes the quantitative XRD parameters of samples. At low Fe loading, the characteristic MFI peaks are preserved, while the relative crystallinity decreases slightly to 95.18%, indicating a modest loss of long-range structural order. The (101) and (303) peaks shift toward higher 2θ value, which is typically associated with lattice distortion. Notably, the FWHM of Fe@S-2 values remain small, suggesting that loading Fe does not cause significant peak broadening and that the MFI crystalline domains remain relatively coherent. At a higher Fe loading (Fe@S-5), the relative crystallinity decreases to 78.510% (e.g., FWHM of the (101) reflection increases to 0.163°), indicating increased structural disorder.

Table 2 Relative crystallinity and XRD peak parameters (2θ, Δ2θ, and FWHM) for the (101) and (303) facets of samples.

Samples	Relative crystallinity (%)	2θ (101)	Δ2θ (101)	FWHM (°2θ) (101)	2θ (303)	Δ2θ (303)	FWHM (303)
S-1	100.00	7.54	0.00	0.146	23.54	0.00	0.147
Fe@S-2	95.18	7.64	+ 0.10	0.138	23.62	+ 0.08	0.131
Fe@S-5	78.51	7.64	+ 0.10	0.163	23.62	+ 0.08	0.140
Fe@S-14	1.77	-	-	-	-	-	-

The FTIR spectra of the samples are shown in **Figure 3**. The vibration band at 450 cm^{-1} is assigned to the Si–O–Si bending vibration. The peak observed at 550 cm^{-1} is attributed to the double-5 ring vibration which is a characteristic band of the MFI framework, and it is not observed for Fe@S-14 [28]. Furthermore, the vibration peak at 800 cm^{-1} is assigned to the symmetric stretching of Si–O–Si in the outer SiO_4 tetrahedron [29]. The peak at 1,108 cm^{-1} is associated with the asymmetric stretching vibration of Si–O–Si in the inner SiO_4 tetrahedron [30,31], while the nearby band at ~1,100 cm^{-1} indicates the presence of Fe–O–Si

bond formed by the Fe species into the silica framework [32]. The vibration band at 1,224 cm^{-1} is assigned to Si–O–Si asymmetric stretching in the outer SiO_4 tetrahedron with the condensed silica network [33]. Moreover, aboard vibration band at 3,400 - 3,500 cm^{-1} is attributed to the stretching vibration of hydroxyl group (–OH), originating from adsorbed water molecules or surface silanol (Si–OH) group. According to IR analysis there are no absorption bands corresponding to iron oxide phases which may be due to low iron content in Fe@S-2 and Fe@S-5 samples.

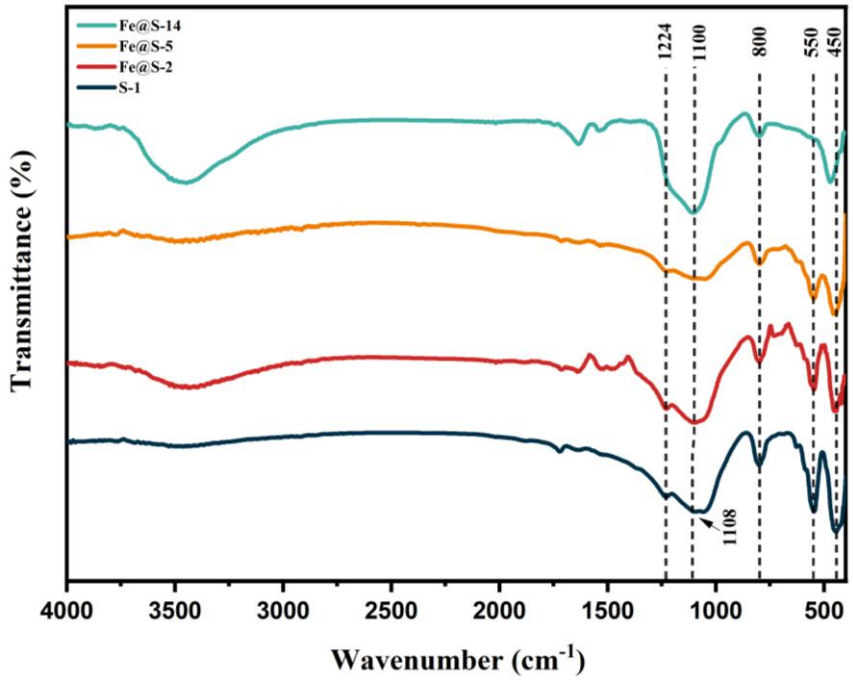

Figure 3 FTIR spectra of S-1 and Fe@Sx synthesized with different Fe molar ratios.

Figure 4 shows the surface morphology and elemental distribution of the Fe@S-5. The Fe@S-5 sample exhibited a typical spherical-like crystal shape, with morphology similar to the structure of MFI-1 type zeolites. This morphology indicates uniform crystal growth and a high structural order, consistent with the XRD results. The addition of Fe led to the formation of spherical morphology with slight surface irregularities due to localized lattice strain induced by the substitution of Fe within the MFI framework. The Fe@S-5 shows a uniform monocrystalline structure with an average particle diameter of 2.8 μm in **Figure 5**. The distribution mapping of elements confirmed the presence of Si, O, and Fe as shown in **Figures 4(b) - 4(f)**. The further elemental mapping exhibits a uniform distribution of Si and O. Additionally, the elemental distribution of the Fe element in Fe@S-5 appears as a dispersed red color, indicating a highly dispersed state and a uniform distribution of iron species in the sample [34].

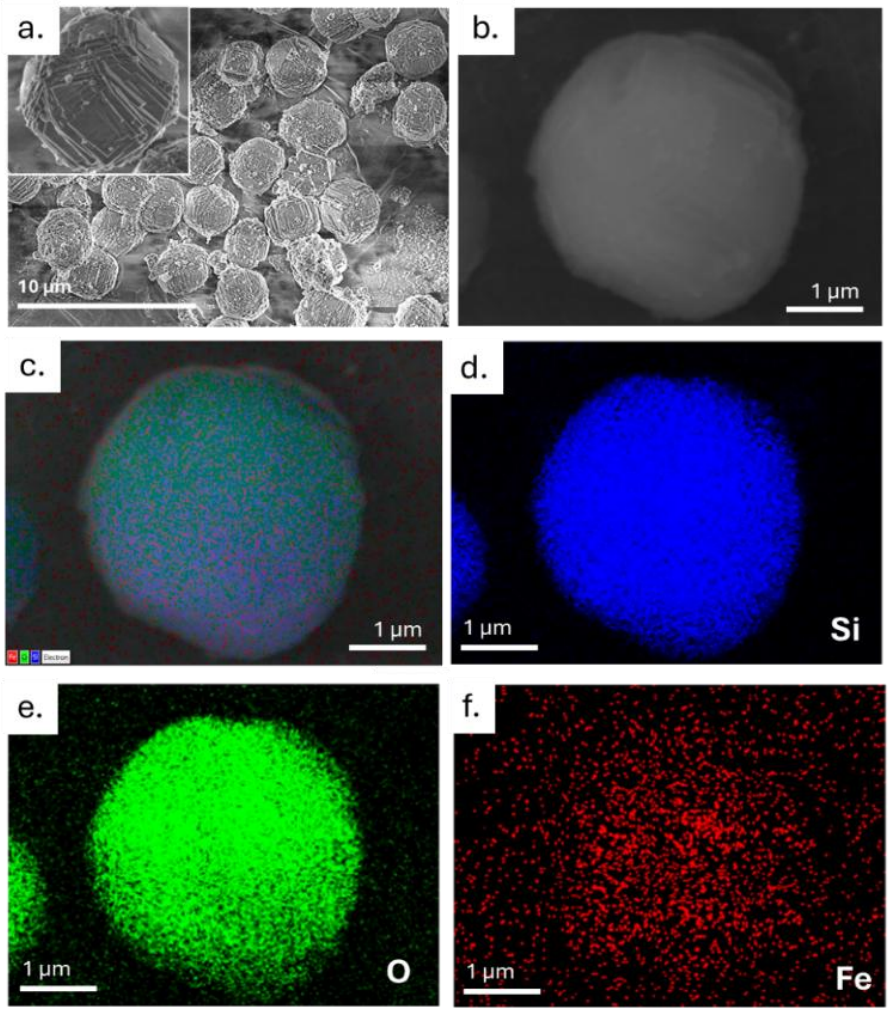

Figure 4 (a) FESEM image of the Fe@S-5; (b) elemental mapping of Fe@silicalite-1 0.005 mol (c) all elements; (d) silicon (Si); (e) oxygen (O); (f) iron (Fe).

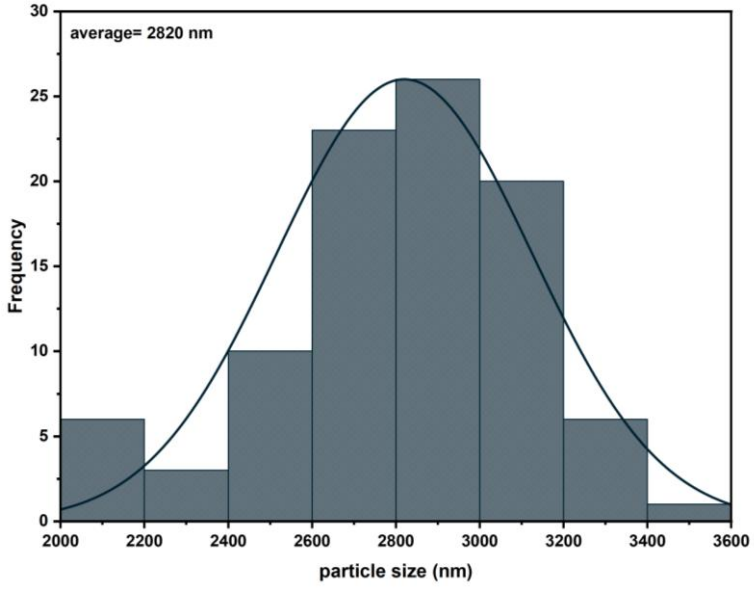

Figure 5 Particle size distribution histogram of Fe@S-5.

The surface area of samples was evaluated using the methylene blue (MB) adsorption method. The calculated specific surface area values are summarized in **Table 3**.

Table 3 Surface area of Fe@S-14, Fe@S-5, Fe@S-2 and S-1 samples.

Samples	Surface area ($m^2 g^{-1}$)
Fe@S-14	174.2
Fe@S-5	150.6
Fe@S-2	154.5
S-1	149.7

Based on the data presented in **Table 3**, the addition of Fe into the S-1 structure significantly affects the surface area of the material. The S-1 exhibits external surface area of 149.7 $m^2 g^{-1}$, which is consistent with the external surface area reported for silicalite-1 (150 $m^2 g^{-1}$) by Liu *et al.* [35]. In comparison, Fe@S-2 and Fe@S-5 show slightly higher external surface area of 154 and 150 $m^2 g^{-1}$, respectively. This trend indicates that Fe associated with the silicate structure may increase surface heterogeneity and provide additional sites for dye adsorption [36]. Meanwhile, the Fe@S-14 exhibits a higher surface area of 174 $m^2 g^{-1}$ and it is supported by XRD data that shows an amorphous phase. The amorphous phase typically has more open and irregular pore structure, which facilitates the diffusion of methylene blue molecules into the porous network [37,38].

Adsorption experiment

Effect of initial concentration of methylene blue

In order to evaluate the effect of the initial dye concentration, methylene blue solutions of 10 - 40 mg L^{-1} were contacted with the adsorbents for 60 min as presented in **Figure 6**. The pure S-1 sample shown in **Figure 6(a)**, exhibits the lowest adsorption capacity of 7.9 mg g^{-1} at 40 mg L^{-1} after 60 min, which is reasonable for all silica relatively hydrophobic MFI surface with limited negatively charged sites available for binding a cationic dye [39]. For silica-based adsorbents, MB adsorption is strongly promoted by deprotonated silanol groups (SiO^-), which provide electrostatic attraction and hydrogen-bonding interactions; therefore, a low accessibility of such sites can limit uptake [40]. Meanwhile, Fe@S-2 and Fe@S-5 exhibit slightly higher adsorption capacities of 9.8 and 8.7 mg g^{-1} at 40 mg L^{-1} respectively shown in **Figure 6 (b,c)**, suggesting that the formation of defect increase the surface heterogeneity [16]. In contrast, the Fe@S-14 shows the highest adsorption capacity of 46 mg g^{-1} at 40 mg L^{-1} shown in **Figure 6(d)**. This enhancement is consistent with the pronounced crystallinity loss/partial amorphization indicated by XRD, which can generate a more open and irregular pore channel and reduce mass-transfer limitations, thereby facilitating molecular diffusion and improving access to available adsorption sites [41,42].

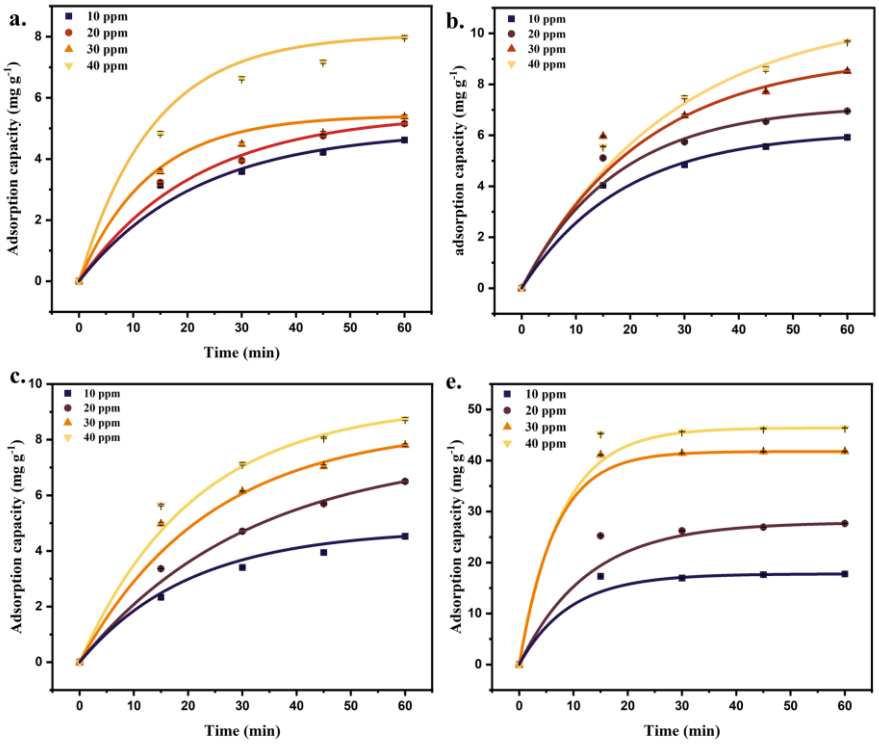

Figure 6 Adsorption capacity of a) S-1, b) Fe@S-2, c) Fe@S-5 and d) Fe@S-14.

Adsorption kinetics

To investigate the adsorption kinetics of methylene blue, the experimental data were fitted using nonlinear pseudo-first order (PFO) and pseudo-second order (PSO) models [43]. Kinetic experiments were conducted over contact time of 0 - 60 min at an initial MB concentration of 30 mg L^{-1}, as shown in **Figure 7**. The nonlinear fitting results and kinetic parameters are summarized in **Table 4**. Based on the analysis of the adsorption kinetic models, the adsorption process of methylene blue on S-1, Fe@S-2, Fe@S-5, and Fe@S-14 are more appropriately described by PSO because it has a higher correlation value R^2 than the PFO model. Notably, Fe@S-14 showed an excellent fit to the PSO model (R^2 = 0.999), indicating that the overall adsorption rate is strongly governed by the availability of adsorption sites and their interactions with MB. Following common interpretation of the PSO model, this behavior is often associated with chemisorption-controlled kinetics [44].

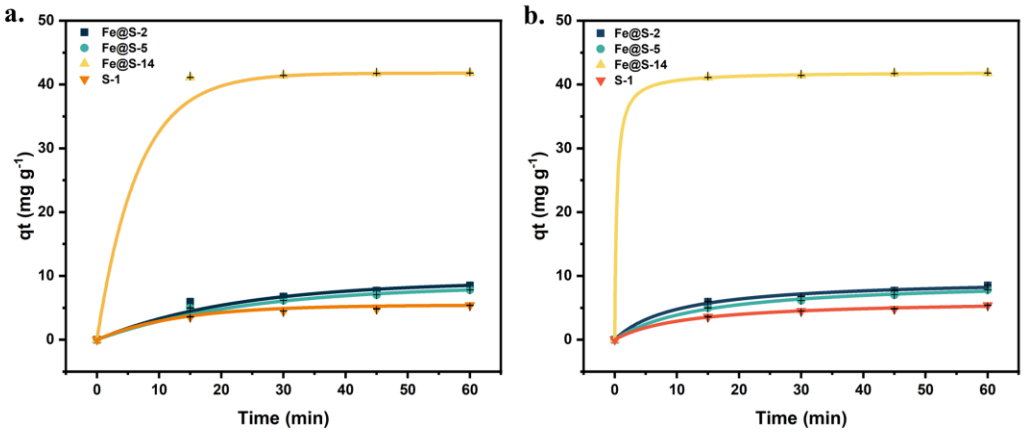

Figure 7 Kinetic models a) pseudo-first order and b) pseudo-second order.

A higher PSO rate constant (K_2) generally indicates that the adsorption process occurs more rapidly, aligning with the corresponding reaction model. The Fe@S-14 exhibits the highest K_2 value of 0.072 g mg^{-1} min^{-1}, indicating a rapid adsorption kinetics. In comparison, S-1, Fe@S-2 and Fe@S-5 show lower K_2 value of 0.014, 0.010 and 0.007 g mg^{-1} min^{-1}, respectively. Consistent with this trend, Fe@S-14 also delivers the highest equilibrium adsorption capacity (q_e) at 41.988 mg g^{-1}, followed by Fe@S-2, Fe@S-5, S-1 with values of 9.602, 9.430 and 6.261 mg g^{-1}, respectively. Methylene blue adsorption typically proceeds via an initial rapid uptake on the external surface, followed by a slower stage controlled by intra particle diffusion into accessible pore. Since MB is cationic dye, its adsorption can be promoted by electrostatic interactions with negatively charged surface sites, such as deprotonated silanol groups (SiO_2^-). It shows that the adsorption process depends not only on the concentration of the adsorbate but also on the chemical interactions between the active groups on the adsorbent and methylene blue, which is typical of the PSO kinetic model [45].

Table 4 Kinetic pseudo first order and pseudo second order model parameter values.

Adsorbent	Pseudo-first order			Pseudo-second order		
	qe exp (mg/g)	K_1 (min^{-1})	R^2	qe exp (mg/g)	K_2 (g mg^{-1} min^{-1})	R^2
Fe@S-2	9.153	0.044	0.932	9.602	0.010	0.990
Fe@S-5	8.496	0.042	0.962	9.430	0.007	0.995
Fe@S-14	41.783	0.152	0.987	41.988	0.072	0.999
S-1	5.434	0.077	0.974	6.261	0.014	0.997

Adsorption isotherms

The Langmuir and Freundlich isotherm models were used to investigate MB adsorption behavior on the prepared adsorbents, as shown in Figure 8 and the corresponding fitting parameters are summarized in **Table 5**. According to the Langmuir model, Fe@S-14 demonstrates an adsorption capacity at 196.248 mg g^{-1}, which is substantially higher than that S-1. However, Fe@S-14 shows a relatively low Langmuir constant at 0.009 L mg^{-1}, suggesting weaker adsorption affinity within the concentration range investigated and indicating that q_{max} may represent an extrapolated value rather than a directly achieved saturation capacity. In contrast, Fe@S-2 and Fe@S-5 exhibit lower q_{max} values of 12.124 and 12.696 mg g^{-1}, respectively, accompanied by higher KL values of 0.083 and 0.054 L mg^{-1}. The Langmuir model provides the better fit for all samples based on the higher R^2 values, suggesting that adsorption is reasonably described by a predominantly monolayer-type uptake on an energetically similar set of sites within the measured concentration range [46].

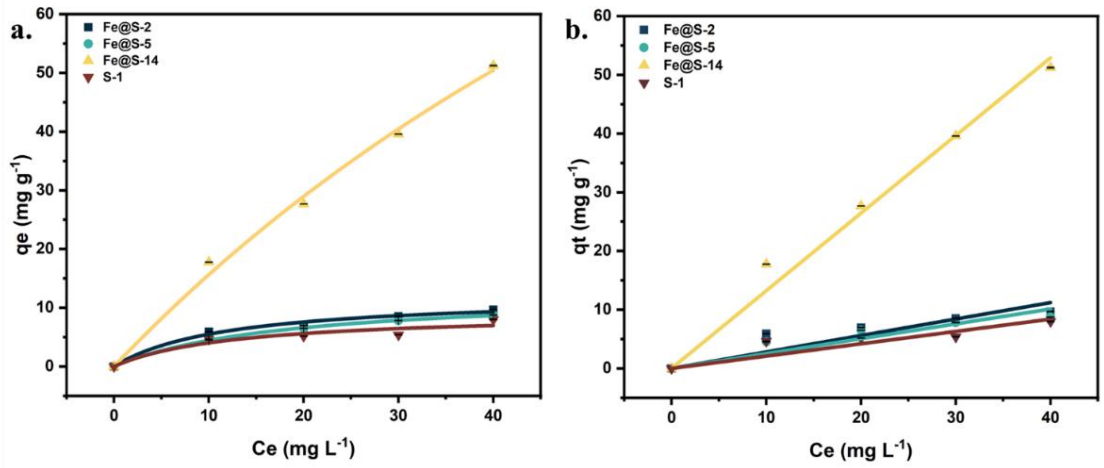

Figure 8 Plot of (a) Langmuir and (b) Freundlich isotherm models.

For Freundlich isotherm model, Fe@S-14 exhibits a K_f value of 1.124 and an *n* value of 0.849. An *n* value close to 1 generally indicates weak to moderate adsorption intensity and a less favorable adsorption process compared with systems showing higher *n* value. This behavior may be associated with surface heterogeneity and non-ideal site distribution arising from particle agglomeration and the presence of amorphous domains in the material [47]. In contrast, the Fe@S-2 shows a more balance adsorption behaviour, with n = 1.503 and K_f = 0.421, suggesting a relatively more favourable adsorption intensity than Fe@S-14 within the investigated concentration range. Meanwhile, the S-1 displays a *n* value of 1.561, however its adsorption capacity was relatively low, suggesting a limited number of adsorption-accessible sites on the silica surface.

Table 5 Parameter values of the Langmuir and Freundlich isotherm model.

Adsorbent	Langmuir				Freundlich		
	Q_{max} (mg/g)	K_L (L/mg)	$\chi 2$	R^2	K_f	n	R^2
Fe@S-2	12.124	0.083	0.236	0.983	0.421	1.503	0.674
Fe@S-5	12.696	0.054	0.007	0.999	0.396	1.567	0.778
Fe@S-14	196.248	0.009	2.509	0.994	1.124	0.849	0.979
S-1	9.233	0.077	0.903	0.919	0.328	1.561	0.671

Tabel 6 Comparative adsorption performance of silica-based materials.

Adsorbent	Silica/precursor	Surface area ($m^2\ g^{-1}$)	MB adsorption performance	Ref.
Silicalite-1	TEOS	-	16.45 mg g^{-1} at 50 mg L^{-1}	[16]
NaX modified SDS	Rice husk	8.3 $m^2\ g^{-1}$	13.48 mg g^{-1} at 250 mg L^{-1}	[48]
Fe_3O_4/ natural zeolite composite	Natural zeolite	-	32.258 mg g^{-1} at 30 mg L^{-1}	[49]
Silicalite-1	Geothermal sludge	149.7 $m^2\ g^{-1}$	7.9 mg g^{-1} at 40 mg L^{-1}	This work
Fe@S-14	Geothermal sludge	174.2 $m^2\ g^{-1}$	46 mg g^{-1} at 40 mg L^{-1}	This work

Table 6 compares the methylene blue (MB) adsorption performance of the present materials with representative zeolite/silica-based adsorbents reported in the literature. As shown, conventional silicalite-1 synthesized from TEOS exhibits an MB uptake of 16.45 mg g^{-1} at an initial concentration of 50 mg L^{-1} [16]. In contrast, the silicalite-1 prepared using geothermal sludge in this work shows lower uptake (7.9 mg g^{-1} at 40 mg L^{-1}), which is reasonable because all-silica MFI materials are relatively hydrophobic and typically provide fewer strong adsorption interactions for cationic dyes without additional surface heterogeneity. Notably, Fe@S-14 demonstrates substantially higher adsorption (46 mg g^{-1} at 40 mg L^{-1}), indicating that Fe modification and the associated structural disorder/partial amorphization can markedly enhance accessible adsorption sites and improve MB surface interactions compared with silicalite-1. Compared with other modified zeolitic adsorbents, NaX modified with SDS shows 13.48 mg g^{-1} even at a much higher MB concentration (250 mg L^{-1}), while an Fe_3O_4/natural zeolite composite achieves 32.258 mg g^{-1} at 30 mg L^{-1} [48]. Beyond adsorption performance, the main advantage of this approach is sustainability due to silica-rich geothermal sludge is employed as a silica source, which reduces dependence on commercial TEOS and enables the upcycling of industrial waste into functional adsorbents.

Conclusions

Geothermal sludge was successfully converted into Fe doped silicalite-1 via hydrothermal synthesis, assisted by an acid leaching pretreatment to obtain a reactive silica precursor. Fe loading markedly

influenced the crystallization behavior, low Fe loading preserved the MFI framework with only a slight reduction in relative crystallinity (Fe@S-2 = 95.81%), whereas excessive Fe loading decreased crystallinity (Fe@S-14 = 1.77%). Despite this structural trade-off, Fe@S-14 exhibited the highest surface area (174 $m^2 g^{-1}$) and delivered the best methylene blue adsorption performance with a value of 46 mg g^{-1}. Kinetic analysis showed that the adsorption data were best described by the pseudo-second order model and equilibrium behavior was reasonably captured by the Langmuir isotherm. Future work should focus on regeneration and multi-cycle stability testing and validating the adsorbent in real textile wastewater containing mixed dyes and competing ions. Overall, these findings highlight geothermal sludge as a sustainable silica feedstock and support the potential use of the resulting Fe-doped silicalite-1 as low-cost adsorbents for dye-contaminated wastewater, particularly relevant to textile effluent and circular-economy adoption at geothermal facilities

Acknowledgements

The authors greatly acknowledge Institut Teknologi Sepuluh Nopember (ITS) for funding this work under the scheme of Penelitian Keilmuan 2025 with contract number 1769/PKS/ITS/2025.

CRediT author statement

Ade Irma Rozafia: Writing-original draft, Visualization, Validation, Investigation. **Bintang Prameswara**: Writing - original draft, Investigation. **Nur Karimah**: Writing - original draft, Validation. **Nor Farida**: Formal analysis, Investigation. **Wahyu Prasetyo Utomo**: Writing - original draft, Validation, Visualization. **Ratna Ediati**: Writing - original draft, Formal analysis. **Aishah Abdul Jalil**: Methodology, Validation, Supervision. **Djoko Hartanto**: Writing - original draft, Validation, Methodology, Funding acquisition, Supervision.

References

[1] A Khaleque, MM Alam, M Hoque, S Mondal, J Bin Haider, B Xu, MAH Johir, AK Karmakar, JL Zhou, MB Ahmed and MA Moni. Zeolite synthesis from low-cost materials and environmental applications: A review. *Environmental Advances* 2020; **2**, 100019.

[2] M Slavova, I Slavov, V Terziev, E Mladenova and B Abrashev. Analysis of the effects of zeolite additions on the properties of battery components: A review article. *Electrochim Acta* 2025; **513**, 145557.

[3] GM Wangi, PW Olupot and RKulabako. Optimization of natural zeolite powder milling parameters to enhance surface area and improve heavy metal adsorption from water. *Discover Applied Sciences* 2025; **7(10)**, 1-34.

[4] J Zang, H Yu, G Liu, M Hong, J Liu and T Chen. Research progress on modifications of zeolite Y for improved catalytic properties. *Inorganics* 2023; **7(10)**, 1-34.

[5] IMS Anekwe, B Oboirien and YM Isa. Effects of transition metal doping on the properties and catalytic performance of ZSM-5 zeolite catalyst on ethanol-to-hydrocarbons conversion. *Fuel Communications* 2024; **18**, 100101.

[6] X Sun, H Qi, Y Jiang, Q Zhao, P Lu, S Chen, C Xing, E Maturura and N Tsubaki. Ultrafast green synthesis of sub-micron Silicalite-1 zeolites by a grinding method. *Journal of Solid State Chemistry* 2022; **310**, 123016.

[7] J Yang, YX Huang, Y Pan and JX Mi. Green synthesis and characterization of zeolite silicalite-1 from recycled mother liquor. *Microporous and Mesoporous Materials* 2020; **303**, 110247.

[8] AM Fard and A Afshar Ebrahimi. Eco-friendly synthesis of ZSM-5 from rice husk ash using top-down modifications for enhancing acetone-to-olefin conversion: Evaluation of catalytic performance and operating conditions. *Fuel* 2025; **386**, 134280.

[9] HTBM Petrus, A Andriani, VSH Sujoto, M Inggrini, M Syauqi, W Astuti, SNA Jenie, KC Wanta, F Anggara, I Perdana, P Mulyono and Y Kusumastuti. High-yield synthesis of silica nanoparticles from geothermal silica via a facile co-precipitation method: Statistical optimization and kinetic analysis. *Particuology* 2025; **106**, 222-235.

[10] M I H S N, C Panatarani, F Faizal, C Mulyana and IM Joni. Synthesis of mesoporous Silica SBA-15 from geothermal sludge. *Materialia* 2023; **27**, 101637.

[11] PU Nzereogu, AD Omah, FI Ezema, EI Iwuoh and A C Nwanya. Silica extraction from rice husk: Comprehensive review and applications. *Hybrid Advances* 2014; **4**, 100111.

[12] SE Lehman and SC Larsen. Zeolite and mesoporous silica nanomaterials: Greener syntheses, environmental applications and biological toxicity. *Environmental Science: Nano* 2014; **1(3)**, 200-213.

[13] FC Rivas, I Rodríguez-Iznaga, G Berlier, DT Ferro, B Concepción-Rosabal and V Petranovskii. *Iron modified natural zeolite as sustainable environmental catalysts: Correlation between iron speciation and catalytic activity in NO-reduction. In*: AE Lakem (Ed.). Vide Leaf, Prime archives in chemistry. Hyderabad, India, 2020, p. 1-28.

[14] Y Zhai, X Zhang, F Wang, G Lv, H Li, T Jiang, Y Wu and M Li. One-step synthesis of high-amount Fe-doped hollow MFI zeolite by Kirkendall effect in the presence of organic acid anions. *Microporous and Mesoporous Materials* 2020; **307**, 110451.

[15] H Guo, L Chen, X Zhang, H Chen and Y Shao. Silicalite-1 zeolite encapsulated Fe nanocatalyst for Fenton-like degradation of methylene blue. *Chinese Journal of Chemical Engineering* 2023; **53**, 251-259.

[16] S Radoor, J Karayil, A Jayakumar, J Parameswaranpillai and S Siengchin. Release of toxic methylene blue from water by mesoporous silicalite-1: Characterization, kinetics and isotherm studies. *Applied Water Science* 2021; **11(7)**, 110.

[17] X Wu, A Nulahong, C Miao, Q Liu, J Li and C Tuo. Solid-phase synthesis of silicalite-1 molecular sieve based on fly ash and its CO_2 adsorption performance. *Greenhouse Gases: Science and Technology* 2024; **14(6)**, 954-976.

[18] N Karimah, RC Andiani, WP Utomo, AI Rozafia, N Farida, A Rosyidah, R Liu, Q Xu and D Hartanto. Factors contributing to reduced photocatalytic activity in Cu-loaded TiO_2/activated carbon composites for methylene blue degradation. *South African Journal of Chemical Engineering* 2025; **54**, 582-596.

[19] G Yuhaneka, AI Rozafia, WP Utomo, A Iryani and D Hartanto. Synthesis of porous g-C_3N_4 and its application as photocatalyst for methylene blue degradation. *Malaysian Journal of Fundamental and Applied Sciences* 2022; **18(4)**, 463-472.

[20] D Hartanto, AB Pambudi, DN Cahyanti and WP Utomo. On the synthesis of ZSM-5 directly from kaolin bangka with aging time. *IOP Conference Series: Materials Science and Engineering* 2019; **588(1)**, 012039.

[21] N Farida, R Purbowati, N Karimah, AI Rozafia, WP Utomo, I Susilo, HY Chung, A Rosyidah, A Soeprijanto and D Hartanto. Marine collagen-driven synthesis of one-dimensional silver nanoparticles. *Materials Letters* 2025; **397**, 138822.

[22] WP Utomo, N Farida, B Aisyah, AA Babgei, N Karimah, A I Rozafia, I Susilo, T Widjaja, H Nur, R Sari, R Liu and D Hartanto. Facile synthesis of flower-like bismuth oxybromide anchored on ZSM-5 for enhanced photocatalytic dye degradation. *South African Journal of Chemical Engineering* 2025; **53**, 386-399.

[23] CA Nunes and MC Guerreiro. Estimation of surface area and pore volume of activated carbons by methylene blue and iodine numbers. *Química Nova* 2011; **34**, 472-476.

[24] K Stone, A M TS Bandara, G Senanayake, and S Jayasekera. Processing of rare earth phosphate concentrates: A comparative study of pre-leaching with perchloric, hydrochloric, nitric and phosphoric acids and deportment of minor/major elements. *Hydrometallurgy* 2016; **163**, 137-147.

[25] S Xu, T J A Slater, H Huang, Y Zhou, Y Jiao, CMA Parlett, S Guan, S Chansai, S Xu, X Wang, C Hardacre and X. Fan. Developing silicalite-1 encapsulated Ni nanoparticles as sintering-/coking-resistant catalysts for dry reforming of methane. *Chemical Engineering Journal* 2022; **446**, 137439.

[26] R Zhao, J Chen, J Liu, J Fan and J Du. Morphologies-controlling synthesis of silicalite-1 and its adsorption property. *Materials Letter* 2015; **139**, 494-497.

[27] W Kellouai, P Judeinstein, M Plazanet, S Baudoin, M Drobek, A Julbe and B Coasne. Gas adsorption in zeolite and thin zeolite layers: Molecular simulation, experiment, and adsorption potential theory. *Langmuir* 2022; **38(18)**, 5428-5438.

[28] Q Liu, Y Fang, C Miao, Z Liao, J Lu, J Li, X Wu and A Nulahong. Preparation of ZSM-5 molecular sieve modified by kaolin and its CO2 adsorption performance investigation. *Microporous and Mesoporous Materials* 2023; **360**, 112678.

[29] J Qi, T Zhao, X Xu, F Li and G Sun. Hydrothermal synthesis of size-controlled silicalite-1 crystals. *Journal of Journal of Porous Materials* 2011; **18(4)**, 509-515.

[30] X Yang, J Chen, H Lai, J Hu, M Fang and X Luo. MOF-derived Co/ZnO@silicalite-1 photocatalyst with high photocatalytic activity. *RSC Advances* 2017; **7(61)**, 38519-38525

[31] YF Yeong, AZ Abdullah, AL Ahmad and S Bhatia. Synthesis, structure and acid characteristics of partially crystalline silicalite-1 based materials. *Microporous and Mesoporous Materials* 2009; **123(1-3)**, 129-139.

[32] J Tao, Y Jia, T Bai, W Huang, Y Cui, Y Zhou and Q Wei. Study on the catalytic performance of Fe in-situ modified small crystallite Silicalite-1 zeolite in Chichibabin condensation reaction. *Journal of Fuel Chemistry and Technology* 2024; **52(9)**, 1280-1289.

[33] M Nawab, S Barot and R Bandyopadhyay. Nano-sized Silicalite-1: Novel route of synthesis, metal impregnation and its application in selective oxidation of toluene. *Journal of Chemical Sciences* 2019; **131(1)**, 2.

[34] H Sun, Y Han, Z Liu, X Zhang, P Wu, P Bai, P Peng and Z Yan. Incorporating iron species into silicalite-1 framework through iminodisuccinate ligand to achieve superior catalytic performance in propane dehydrogenation. *Renewables* 2025; **3(2)**, 87-98.

[35] G Liu, J Liu, N He, C Miao, J Wang, Q Xin and H Guo. Silicalite-1 zeolite acidification by zinc modification and its catalytic properties for isobutane conversion. *RSC Advances* 2018; **8(33)**, 18663-18671.

[36] O Sophiphun, S Chanprame and C Laksana. Evaluation of synthesis method of fe loaded amorphous silica on the adsorption of glyphosate. *Current Applied Science and Technology* 2022; **23(3)**, 10-55003.

[37] M Turchi, S Galmarini and I Lunati. Learning adsorption patterns on amorphous surfaces. *Journal of Chemical Theory and Computation* 2024; **20(17)**, 7597-7610.

[38] C Strangfeld, P Wiehle and SM Munsch. About the dominance of mesopores in physisorption in amorphous materials. *Molecules* 2021; **26(23)**, 7190.

[39] T Hongo, M Moriura, Y Hatada and H Abiko. Simultaneous methylene blue adsorption and ph neutralization of contaminated water by rice husk ash. *ACS Omega* 2021; **6(33)**, 21604-21612.

[40] N Yuan, H Cai, T Liu, Q Huang and X Zhang. Adsorptive removal of methylene blue from aqueous solution using coal fly ash-derived mesoporous silica material. *Adsorption Science & Technology* 2019; **37(3-4)**, 333-348.

[41] X Jia, W Khan, Z Wu, J Choi and ACK Yip. Modern synthesis strategies for hierarchical zeolites: Bottom-up versus top-down strategies. *Advanced Powder Technology* 2019; **30(3)**, 467-484.

[42] S Xu, K Zheng, CR Boruntea, DG Cheng, F Chen, G Ye, X Zhou and MO Coppens. Surface barriers to mass transfer in nanoporous materials for catalysis and separations. *Chemical Society Reviews* 2023; **52(12)**, 3991-4005.

[43] Y Bakhtaoui, M Ben Ali, M Ouakki, O El Khattabi, N El Azzouzi and B Srhir. Efficient adsorption of methylene blue onto raw olive pomace from Moroccan industrial oil mills: Linear and nonlinear isotherm and kinetic modeling with error analysis. *Next Materials* 2025; **9**, 101072.

[44] MA Darweesh, MY Elgendy, MI Ayad, AM Ahmed, NMK Elsayed and WA Hammad. Adsorption isotherm, kinetic, and optimization studies for copper (II) removal from aqueous solutions by banana leaves and derived activated carbon. *South African Journal of Chemical Engineering* 2022; **40**, 10-20.

[45] NW Sabry, I Naeem, SA Hassanien, O Abuzalat and A Baraka. Alkali-treatment of Lupine peels for valorizing adsorption of organic cationic pollutants from wastewater: Kinetics, isotherm, thermodynamic, regeneration, and mechanism. *Next Materials* 2025; **8**, 100568.

[46] GS Aljeddani, RM Alghanmi and RA Hamouda. Study on the isotherms, kinetics, and thermodynamics of adsorption of crystal violet

dye using Ag-NPs-loaded cellulose derived from peanut-husk agro-waste. *Polymers* 2023; **15(22)**, 4394.

[47] I Abdul-Gafaru, SJ Cobbina and K Michael. Green-synthesized magnetic iron oxide nanoparticles for the adsorptive removal of CD2+ and PB2+ from aqueous solution. *Discover Water* 2025; **5(1)**, 92.

[48] S Zharylkan, S Sultakhan, M Suleimenova, S Azat, Y Sailaukhanuly, M Tulepov and Z Tauanov. Engineered science enhanced adsorption of mercury and methylene blue using silver and surface modified zeolite-NaX derived from Rice Husk. *Engineered Science* 2024; **31**, 1241.